We are IntechOpen,
the world's leading publisher of
Open Access books
Built by scientists, for scientists

6,900
Open access books available

186,000
International authors and editors

200M
Downloads

Our authors are among the

154
Countries delivered to

TOP 1%
most cited scientists

12.2%
Contributors from top 500 universities

CLARIVATE ANALYTICS
BOOK CITATION INDEX
INDEXED

WEB OF SCIENCE™

Selection of our books indexed in the Book Citation Index
in Web of Science™ Core Collection (BKCI)

Interested in publishing with us?
Contact book.department@intechopen.com

Numbers displayed above are based on latest data collected.
For more information visit www.intechopen.com

Electronic Properties of Carbon Nanostructures

Jan Smotlacha and Richard Pincak

Additional information is available at the end of the chapter

Abstract

The carbon nanostructures are perspective materials for the future applications. This has two reasons: first, the hexagonal atomic structure, which enables a high molecular variability by placing different kinds of the defects, and second, good electronic properties that can be modified for the purpose of the concrete applications with the help of the defects and of the chemical ingredients. Many kinds of the nanostructures are investigated. Here, the properties of less common forms are examined—the graphitic nanocone and graphitic wormhole.

Keywords: graphene, graphitic wormhole, graphitic nanocone, spin-orbit coupling, zero modes

1. Introduction

The carbon nanostructures are the materials whose molecular structure is derived from graphene—the hexagonal carbon plain lattice (**Figure 1**). Because of their electronic structure, they are the promising materials for the construction of nanoscale devices (quantum wires, nonlinear electronic elements, transistors, molecular memory devices, or electron field emitters) and the inventions in the material science.

The planar geometry of the molecular surface is disrupted by the disclinations in the molecular structure that are most often presented by the pentagons and the heptagons in the hexagonal lattice. This change of the geometry is manifested by the positive or the negative curvature, respectively, that can be enlarged by the supply of higher number of the defects. In this way,

by the supply of 1–5 pentagonal defects, we get conical structures with different values of the vortex angle (**Figure 2**).

One more defect can be added and a nanotube is created. This nanostructure can be considered closed as well as opened, i.e., without the cap that contains the pentagonal defects. The second case is more common (**Figure 3**, left part). The number of the defects can be increased up to 12, and in this way, a completely closed, spherical nanostructure arises (fullerene—**Figure 3**, middle part).
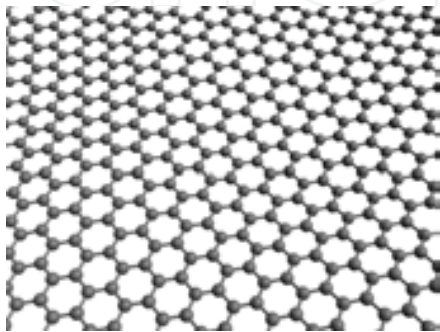
**Figure 1.** Hexagonal carbon plain lattice.

Figure 2. Conical nanostructures with different numbers of pentagonal defects in the tip.
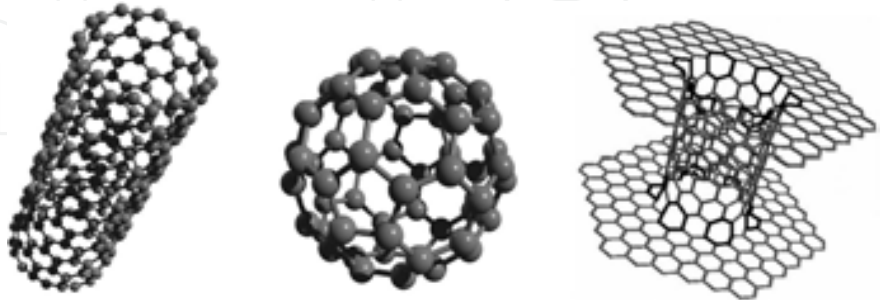
Figure 3. Different kinds of graphene nanostructures: nanotube (left), fullerene (middle), wormhole (right).

Analogical manipulations with the graphene lattice can be made by the supply of the heptagonal defects (**Figure 4**). For the case of 12 heptagonal defects, if they are placed appropriately, the wormhole structure is created (**Figure 3**, right part).
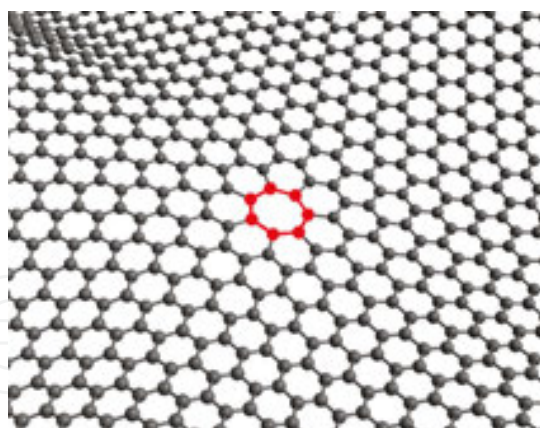
Figure 4. Hexagonal lattice disclinated by one heptagonal defect.

A lot of other variants of the graphitic nanostructures can be created using different combinations of the pentagonal and the heptagonal defects. Some of them are presented in **Figure 5**.

Figure 5. Less common forms of the graphene nanostructures: triple-walled nanotube (left), pillared graphene (middle), nanotoroid (right).

We investigate the electronic properties of several kinds of the carbon nanostructures. After the explanation of the computational methods, we demonstrate how to utilize these methods for the purpose of the investigation of graphene and some simple forms of the nanostructures —different kinds of nanoribbons and their modifications. Then, we will concentrate on the calculation of the properties of more complicated forms—the graphitic nanocone [1–3] and the graphitic wormhole [4–6]. In the first case, we consider the influence of the additional effects like the spin-orbit coupling (SOC) and the boundary effects coming from the finite size and from the extreme curvature of the surface geometry in the tip. In the second case, we investigate the effects that arise in the place of the wormhole bridge. Here, two additional effects appear: first, the SOC arising in the connecting nanotube and second, the increase of the electron mass due to relativistic effects coming from the extreme curvature of the surface geometry. As a result, the chiral massive electrons should be observed.

2. Computational formalism

The electronic structure can be characterized by the density of states (DOS)—the number of the electronic states per the unit interval of energies. This quantity can be used as the measure

of the density of the electrons and generally we can say that the higher value of DOS, the higher conductivity. With the help of DOS, the electric field can be calculated as well. Besides DOS, one more quantity is defined—the local density of states (LDOS). It is DOS related to the unit area of the molecular surface or to the unit area of the surface in the space of the wave vector $\vec{k}$. Then, the quantities depend on the variables as follows:

$$DOS = DOS(E), \quad LDOS = LDOS(E, \vec{r}), \quad \text{resp.} \quad LDOS = LDOS(E, \vec{k}). \tag{1}$$

Two methods are used for the calculation of LDOS. The first one is used for the periodical structures with the planar geometry (plain graphene, nanotubes, nanoribbons, etc.), the second one is used for the structures that are aperiodical or that have the curved geometry (fullerene, nanocone, wormhole, nanotoroid, etc.). We outline here the base of these methods. Both the methods start on solving the Schrödinger equation for the electron bounded on the molecular surface

$$\hat{H}\psi = E\psi. \tag{2}$$

Here,

$$\hat{H} = \frac{\hat{k}^2}{2m} + \hat{V}(\vec{r}) + \hat{U}(\vec{r}), \tag{3}$$

$\hat{V}$ representing the potential of the periodic crystal, $\hat{U}$ representing the external potential that is responsible for the curvature.

2.1. Periodical structures with planar geometry

For the periodical structures, the external potential in Eq. (3) is zero, and the carbon lattice can be divided into several sublattices, each containing equivalent atomic sites. We can denote the sites corresponding to the different sublattices as A, B, C, ... or A_1, A_2, A_3, ... We can find a unit cell—the smallest possible cell in the structure that contains all possible inequivalent atomic sites (**Figure 6**).

In the case of graphene, the wave function, which solves Eq. (2), can be expressed as in references [7, 8]

$$\psi = C_A \psi_A + C_B \psi_B, \tag{4}$$

where the components ψ_A, ψ_B correspond to the particular sublattices. In the tight-binding approximation, we postulate the solution in the form

$$\psi_{A(B)} = \sum_{A(B)} \exp[i\vec{k} \cdot \vec{r}_{A(B)}] X(\vec{r} - \vec{r}_{A(B)}), \tag{5}$$

where $X(\vec{r})$ is the atomic orbital function. The overlap is zero, i.e.,

$$\int X^*(\vec{r} - \vec{r}_A) X(\vec{r} - \vec{r}_B) d\vec{r} = 0.$$

(6)

By the substitution of the solution in Eq. (5) into the Schrödinger equation (Eq. (2)), multiplying it by $\psi^\dagger$ and making the integration over $\vec{r}$, we create the expressions
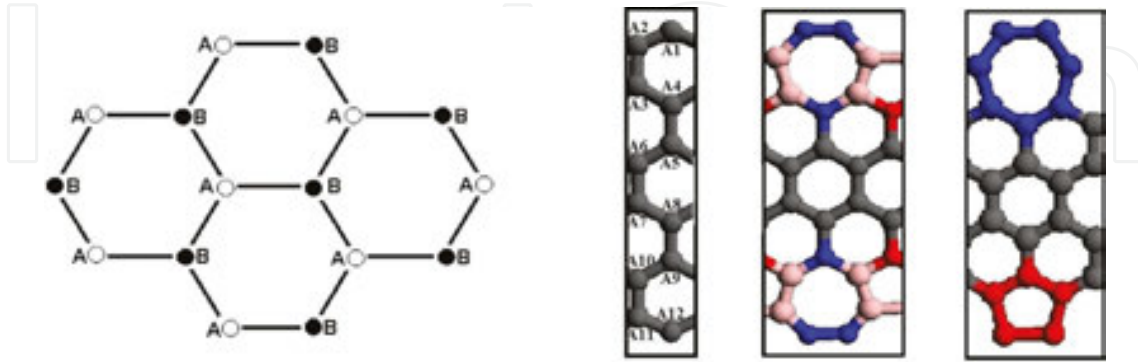
Figure 6. Unit cells for different periodical structures: graphene (left), different kinds of nanoribbons (right). The graphene structure is considered to be infinite in 2D, the nanoribbons are considered to have final width and the second size is infinite as well.

$$H_{ab} = \int \psi_a^* H \psi_b d\vec{r}, \quad S = \int \psi_A^* \psi_A d\vec{r} = \int \psi_B^* \psi_B d\vec{r}, \quad a,b \equiv A, B.$$

(7)

If we suppose that the functions X are normalized so that $\int X^*(\vec{r} - \vec{r}_{A(B)}) X(\vec{r} - \vec{r}_{A(B)}) d\vec{r} = 1$, then S gives the number of the unit cells in the nanostructure. Now, the Schrödinger equation is transformed into the matrix form

$$\begin{pmatrix} H_{AA} & H_{AB} \\ H_{BA} & H_{BB} \end{pmatrix} \begin{pmatrix} C_A \\ C_B \end{pmatrix} = ES \begin{pmatrix} C_A \\ C_B \end{pmatrix}.$$

(8)

The eigenvalues of the matrix in this equation are the energy eigenvalues, and they create the electronic spectrum. For this purpose, first, we need to determine the values of the matrix elements H_{ab}. From their definition follows

$$H_{ab} = \int \psi_a^* H \psi_b d\vec{r} = \sum_{a,b} \exp\left[-i\vec{k} \cdot (\vec{r}_A - \vec{r}_B)\right] \int X^*(\vec{r} - \vec{r}_a) H X(\vec{r} - \vec{r}_b) d\vec{r}$$

$$= \sum_{a,b} \exp\left[-i\vec{k} \cdot (\vec{r}_A - \vec{r}_B)\right] \gamma_{ab},$$

(9)

where γ_{ab} ab denotes the corresponding hopping integral. The eigenvalues are labeled by $\vec{k}$ and in the nearest-neighbor approximation, they can be expressed as

$$E(\vec{k}) = \pm \gamma_0 \sqrt{1 + 4\cos^2 \frac{k_y a}{2} + 4\cos \frac{k_y a}{2} \cos \frac{k_x a \sqrt{3}}{2}},$$

(10)

where $\gamma_0 = \gamma_{AA} = \gamma_{BB}$ is the hopping integral for the nearest neighboring atoms and $a = 2.46A$ is the distance between the next-nearest atomic neighbors. DOS and LDOS are then defined as

$$DOS(E) = -\frac{1}{\pi}\lim_{\omega \to 0} \mathrm{Im} \int \frac{d\vec{k}}{E - E(\vec{k}) + i\omega}, \qquad LDOS(E,\vec{k}) = \delta(E - E(\vec{k})). \qquad (11)$$

The corresponding graphs of electronic spectrum and DOS are given in **Figure 7**. We see that for zero energy, the density of states has zero value. This property is typical for the semimetallic nanostructures. For the metallic nanostructures, a peak appears for zero energy. In the first case, a gap is present around zero in the electronic spectrum. Its width can be influenced by the additional defects in the hexagonal structure or by the chemical admixtures and in this way, a material with the predefined properties can be synthesized. In the second case, the gap around zero energy is absent.
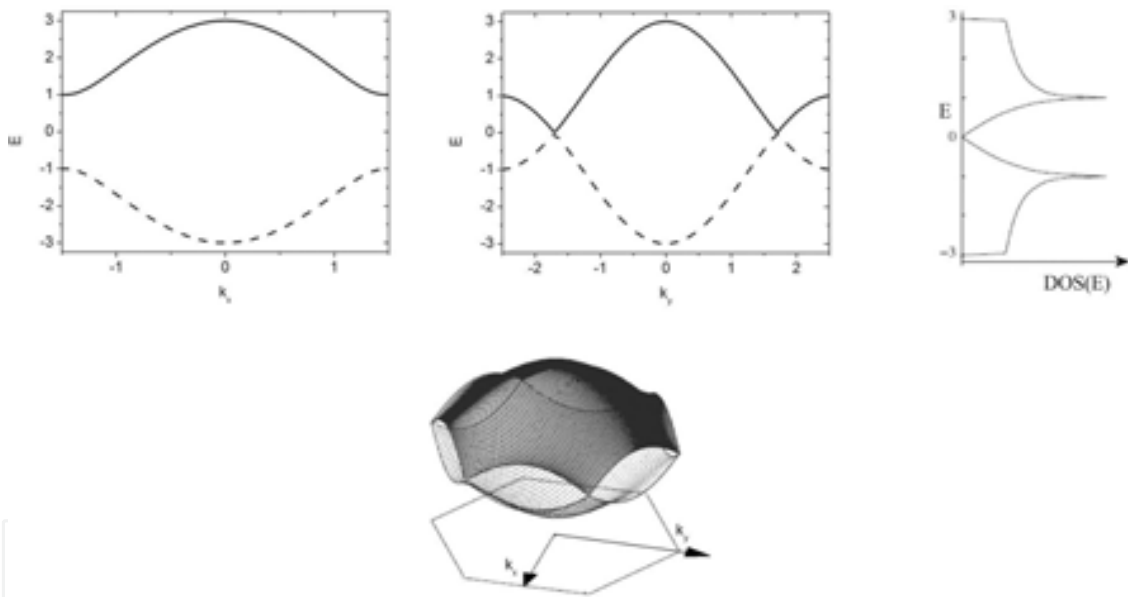

Figure 7. The electronic spectrum for $k_y = 0$ (left) and $k_x = 0$ (middle) and the density of states (right) of graphene. The solid and dashed lines correspond to the positive and the negative energy values, respectively. In the bottom, we see the form of the electronic spectrum for an arbitrary value of the wave vector.

In a similar way, but with a more complicated structure of the wave function in Eq. (4) and for a larger size of the matrix in Eq. (8), the electronic spectrum and DOS can be found for other nanostructures like the nanoribbons in the right side of **Figure 6** [9].

The results we see in **Figure 8**. In the left part, the shape of the segment of the concrete nanoribbon is present. The plot of the electronic spectrum and DOS are given in the middle and in the right part, respectively. The direction of the wave vector $\vec{k}$ is considered longitudinal.

The upper part corresponds to the nanoribbon with zigzag edges [10] and with 12 atomic sites in the unit cell (see **Figure 6**). That is why the size of the appropriate matrix in Eq. (8) would be 12 × 12 and its spectrum contains 12 eigenvalues. This corresponds to 12 lines in the graph of the electronic spectrum. The graph of DOS shows a zero energy peak that signalizes the metallicity of this kind of nanostructure. It is a typical property for the zigzag nanoribbons unlike the armchair nanoribbons [10].
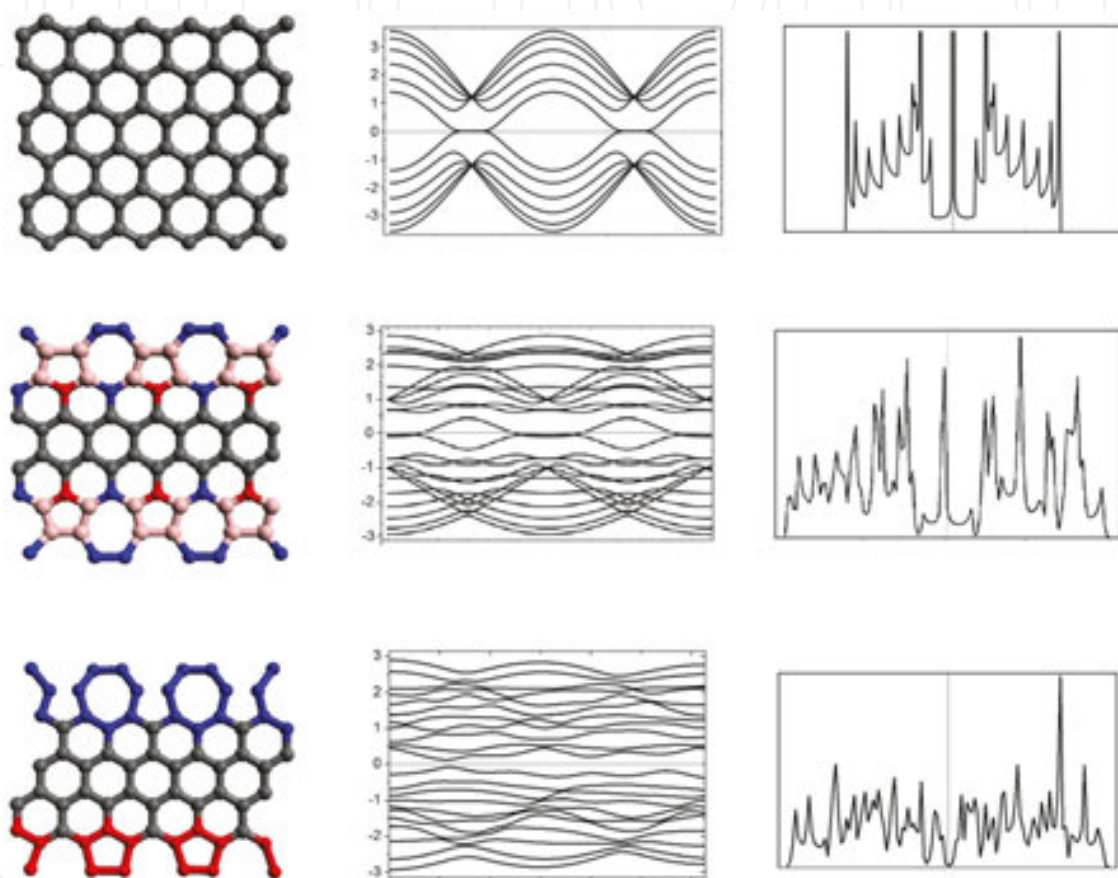
Figure 8. Electronic spectrum and DOS of different kinds of nanoribbons.

The middle and the bottom part correspond to some modifications of the previous form—the nanoribbon with the reconstructed edges. This causes the enlargement of the unit cell (**Figure 6**) and, consequently, a more complicated structure of the electronic spectrum. The metallic properties depend on the concrete kind of the modification: for the nanostructure in the middle part, the zero energy peak in DOS is preserved, whereas it disappears for the nanostructure in the bottom part. Furthermore, in the first case, the electronic spectrum gets a more complicated structure—the number of the Dirac points, where the lines are crossing, is doubled. This feature remains and strengthens for the larger width: in **Figure 9**, the form of the electronic spectrum is depicted for the same kind of the nanostructure and its width is three times larger.

2.2. Structures with curved geometry

For the curved structures, the nontrivial geometry is described by the external potential $U(\vec{r})$ in Eq. (3). Because of the aperiodicity, the eigenvalues cannot be labeled by the wave vector $\vec{k}$. Nevertheless, the solution of the Schrödinger equation (Eq. (2)) can be expressed with the help of the solutions for the previous case as so labeling by the wave vector will still play a key role in the following procedure.
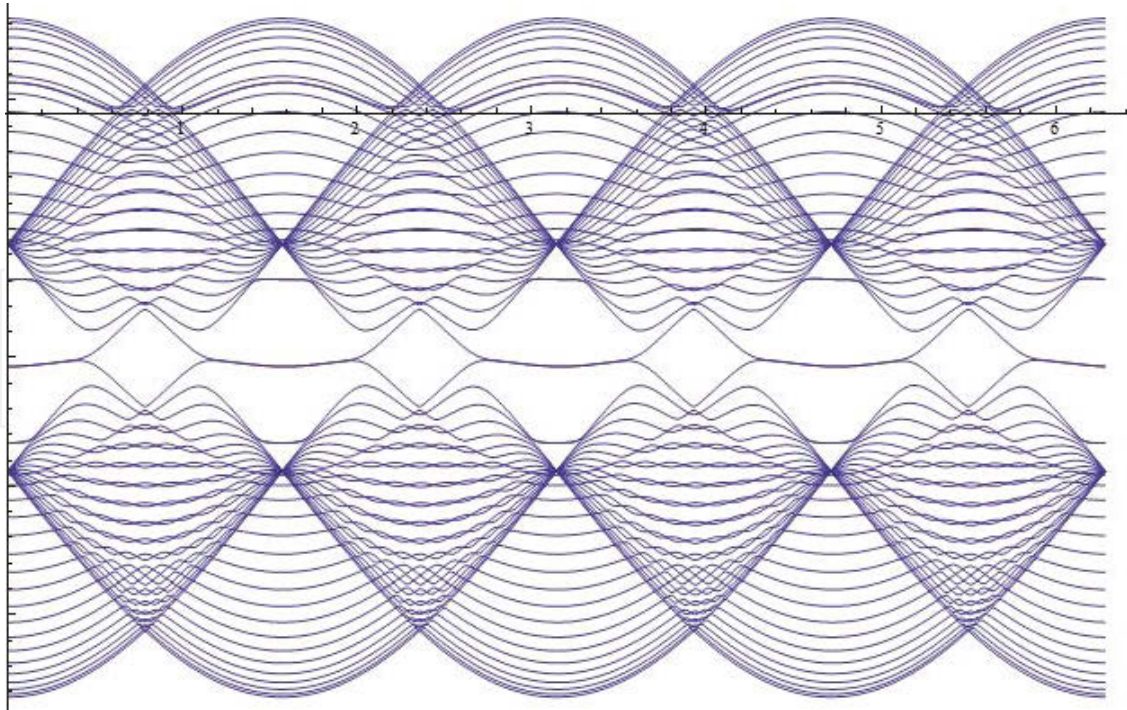
$$\Psi(\vec{r}) = \int d\vec{k}\,\psi_{\vec{k}}(\vec{r}),$$

(12)

For the purpose of the calculations, we express the wave function that solves Eq. (2) in the case of zero external potential in the form of the so-called "Luttinger–Kohn base" [11]:

$$\psi_{\vec{k}}(\vec{r}) = f_A(\vec{\kappa})e^{i\vec{K}\cdot\vec{r}}\psi_A(\vec{K},\vec{r}) + f_B(\vec{\kappa})e^{i\vec{K}\cdot\vec{r}}\psi_B(\vec{K},\vec{r}),$$

(13)

where $\vec{\kappa} = \vec{k} - \vec{K}$, $\vec{K}$ being the Dirac point and $E(\vec{k})$ is the appropriate eigenvalue for the zero external potential. After the substitution of this expression into Eq. (12), we get

$$\Psi(\vec{r}) = \int d\vec{\kappa}\left(f_A(\vec{\kappa})e^{i\vec{K}\cdot\vec{r}}\psi_A(\vec{K},\vec{r}) + f_B(\vec{\kappa})e^{i\vec{K}\cdot\vec{r}}\psi_B(\vec{K},\vec{r})\right).$$

(14)

Figure 9. Electronic spectrum for extra wide nanoribbon with reconstructed edges.

This wave function will be substituted into Eq. (3). In reference [12], a sequence of steps is described whose result is the transformation of this equation to a two-dimensional (2D) Dirac-like equation for the massless fermion. In the practical calculations, a suitable choice of the coordinates is useful. In our case, we will suppose the rotational symmetry. Then, we perform the transformation of the coordinates: $(x, y, z) \to (\xi, \varphi)$, where φ is the angular coordinate. Then, the resulting Dirac-like equation will have the form [13, 14]

$$i\sigma^{\alpha} e_{\alpha}^{\mu} [\partial_{\mu} + \Omega_{\mu} - i a_{\mu} - i a_{\mu}^{W} - i A_{\mu}] \Psi = E\Psi. \tag{15}$$

The meaning of the particular terms is the following: e_{α}^{μ}, the zweibein, is connected with metric and using the corresponding tensor, it can be defined as

$$g_{\mu\nu}(x) = e_{\mu}^{\alpha}(x) e_{\nu}^{\beta}(x) \eta_{\alpha\beta}. \tag{16}$$

Here, $\eta_{\alpha\beta}$ is the metric of the plain space without curvature. Next term, Ω_{μ}, which is the spin connection in the spinor representation, is defined as $\Omega_{\mu} = \frac{1}{8}\omega_{\mu}^{\alpha\beta}[\sigma_{\alpha}, \sigma_{\beta}]$. Here, ω_{μ} is a more usual form of the spin connection. For its definition, we have to stress that the rotational symmetry is supposed. Then, it has the form

$$\omega_{\varphi}^{12} = -\omega_{\varphi}^{21} = 1 - \frac{\partial_{\xi}\sqrt{g_{\varphi\varphi}}}{\sqrt{g_{\xi\xi}}} = 2\omega, \qquad \omega_{\xi}^{12} = \omega_{\xi}^{21} = 0. \tag{17}$$

It remains to explain the sense of the gauge fields a_{μ}, a_{μ}^{W}, A_{μ}. First two of them ensure the circular periodicity. Their form is

$$a_{\varphi} = N/4, \qquad a_{\varphi}^{W} = -\frac{1}{3}(2m + n), \tag{18}$$

where N is the number of defects and (n,m) is the chiral vector. The last term, A_{μ}, represents one possible additional effect—the magnetic field.

The rotational symmetry enables to find the solution of Eq. (15) with the help of the substitution

$$\Psi^{T} = \begin{pmatrix} F_1 \\ F_2 \end{pmatrix} = \frac{1}{\sqrt[4]{g_{\varphi\varphi}}} \begin{pmatrix} u_j(\xi) e^{i\varphi j} \\ v_j(\xi) e^{i\varphi(j+1)} \end{pmatrix}, \qquad j = 0, \pm 1, \ldots, \tag{19}$$

from which we get the system

$$\frac{\partial_{\xi} u_j}{\sqrt{g_{\xi\xi}}} - \frac{\tilde{j}}{\sqrt{g_{\varphi\varphi}}} u_j = Ev, \qquad -\frac{\partial_{\xi} v_j}{\sqrt{g_{\xi\xi}}} - \frac{\tilde{j}}{\sqrt{g_{\varphi\varphi}}} v_j = Eu. \tag{20}$$

Here,

$$\tilde{j} = j + 1/2 - a_\varphi - a_\varphi^W - A_\varphi.$$ (21)

From the solution, LDOS is defined as the square of the absolute value of the wave function. In this case, we get it as the sum of squares of the absolute values of its ξ-components:

$$LDOS(E,\xi) = |u(E,\xi)|^2 + |v(E,\xi)|^2 .$$ (22)

3. Properties of the graphitic nanocone

The graphitic nanocone is a nanostructure that can be created from the plain graphene by the insertion of the pentagonal defects into the hexagonal structure. The number of these defects can vary from one to five. In this way, the conical tip arises and its smoothness and the vortex angle are given by the number of the defects and their placement. Then, the real geometry of the graphitic nanocone and the pure conical geometry are different (**Figure 10**, left part). The value of the vortex angle φ for the purely conical geometry can be calculated as

$$\sin\frac{\varphi}{2} = 1 - \frac{N}{6},$$ (23)

where N is the number of the pentagonal defects in the conical tip.

The electronic structure of the graphitic nanocone with purely conical geometry and without any additional effects was investigated in reference [15]. There, the solution of Eq. (15) for this case is derived. Here, using the gauge field theory approach, we introduce the results of the calculations in different approximations: the nanocone with purely conical geometry influenced by the SOC [1] and the same case with the additional effect of the Coulomb interaction coming from the charge placed into the conical tip [3]. The reason is following: it is one of the possibilities how to simulate the real geometry in the conical tip.

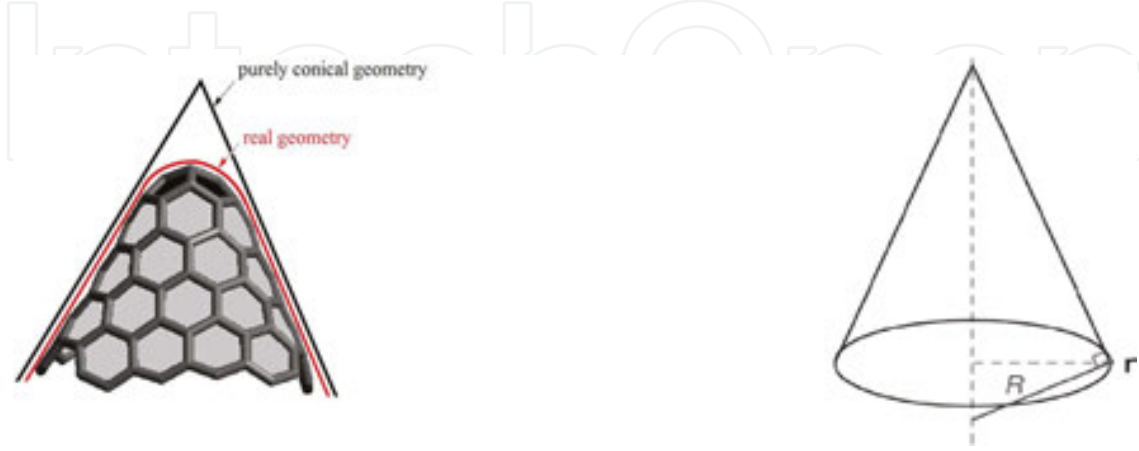### 3.1. Electronic structure influenced by the spin-orbit coupling

In the case of the purely conical structure, this form is assigned to the Hamiltonian in the Schrödinger equation (Eq. (2)) [15]:

$$\hat{H}_0 = \begin{pmatrix} H_1 & 0 \\ 0 & H_{-1} \end{pmatrix} \qquad \hat{H}_{0s} = i\hbar v_F \left\{ \tau^y \partial_r - \tau^x r^{-1} \left[(1-\eta)^{-1} \left(s\partial_\varphi - \frac{3}{2} i\eta \right) - \frac{1}{2}\tau^z \right] \right\}.$$ (24)

In this equation, v_F is the Fermi velocity, $s = \pm 1$ denotes the value of the K spin, $\eta = N/6$, τ^x, τ^y, τ^z are the Pauli matrices—these matrices have nothing to do with SOC. The points on the surface are described by the coordinates r and φ. The value of r is given by the distance from the tip (see **Figure 10**, right part).

SOC is incorporated using the substitutions [1]

$$\partial_r \rightarrow \partial_r - \frac{\delta\gamma'}{4\gamma R}\sigma_x(\vec{r}), \qquad i\partial_\varphi \rightarrow i\partial_\varphi + s(1-\eta)A_y\sigma_y, \qquad (25)$$

purely conical geometry

real geometry

Figure 10. Left: the deviation of the geometry of the graphitic nanocone from the geometry of the real nanocone. Right: The notation of the variables in the nanocone.

where $R = \frac{(1-\eta)r}{\sqrt{\eta(2-\eta)}}$, $A_y = s\frac{2\delta p}{(1-\eta)}\sqrt{\eta(2-\eta)}$. Here, in the analogy to the case of the nanotube, R represents the curvature [16] (the geometrical meaning is also presented in **Figure 10**, right part), A_y is connected with the curvature of the carbon bonds. Next, γ and γ' represent the nearest neighbor and the next-nearest neighbor hopping integrals, respectively, and $\sigma_x(\vec{r}) = \sigma^x\cos\varphi - \sigma^z\sin\varphi$. Here, σ^x, σ^y, σ^z are the Pauli matrices, but (unlikely the τ matrices) this time they are connected with SOC. The parameters p and δ are connected with the hopping integrals and the atomic potential, respectively. Their closer explanation can be also found in reference [16]. The following choice of their values was used: δ is of the order between 10^{-3} and 10^{-2}, $\frac{\gamma'}{\gamma} \sim \frac{8}{3}$, $p \sim 0.1$. After making the transformation $\hat{H}_s \rightarrow e^{i\frac{\sigma_y}{2}\varphi}\hat{H}_s e^{-i\frac{\sigma_y}{2}\varphi}$, which transforms the coordinate frame into the local coordinate frame, the final form of the Hamiltonian is

$$\hat{H}_s = \hbar v_F \begin{pmatrix} 0 & -\partial_r + i\frac{1}{r}\xi_x\sigma_x(\vec{r}) - \frac{is\partial_\varphi}{(1-\eta)r} - \frac{A_y}{r}\sigma_y - \frac{3\eta}{2(1-\eta)r} - \frac{1}{2r} \\ \partial_r - i\frac{1}{r}\xi_x\sigma_x(\vec{r}) - \frac{is\partial_\varphi}{(1-\eta)r} - \frac{A_y}{r}\sigma_y - \frac{3\eta}{2(1-\eta)r} + \frac{1}{2r} & 0 \end{pmatrix}. \qquad (26)$$

It includes the strength of SOC through the parameters ξ_x, ξ_y:

$$\xi_x = \frac{\delta\gamma'\sqrt{\eta(2-\eta)}}{4(1-\eta)\gamma}, \qquad \xi_y = A_y + \frac{1}{2(1-\eta)}. \tag{27}$$

Now, the equation

$$\hat{H}_s\psi(r,\varphi) = E\psi(r,\varphi) \tag{28}$$

will be solved for the calculation of LDOS. Similarly as in Eq. (19), we can do the following factorization due to the rotational symmetry:

$$\psi(r,\varphi) = e^{ij\varphi}\begin{pmatrix} f_{j\uparrow}(r) \\ f_{j\downarrow}(r) \\ g_{j\uparrow}(r) \\ g_{j\downarrow}(r) \end{pmatrix} \tag{29}$$

It changes the equation into the form

$$\begin{pmatrix} 0 & 0 & \partial_r + \dfrac{F}{r} & -\dfrac{i}{r}C \\ 0 & 0 & -\dfrac{i}{r}D & \partial_r + \dfrac{F}{r} \\ -\partial_r + \dfrac{F-1}{r} & \dfrac{i}{r}D & 0 & 0 \\ \dfrac{i}{r}C & -\partial_r + \dfrac{F-1}{r} & 0 & 0 \end{pmatrix}\begin{pmatrix} f_{j\uparrow}(r) \\ f_{j\downarrow}(r) \\ g_{j\uparrow}(r) \\ g_{j\downarrow}(r) \end{pmatrix} = E\begin{pmatrix} f_{j\uparrow}(r) \\ f_{j\downarrow}(r) \\ g_{j\uparrow}(r) \\ g_{j\downarrow}(r) \end{pmatrix}. \tag{30}$$

Next parameters appearing in this equation are

$$F = \frac{sj}{1-\eta} - \frac{3}{2}\frac{\eta}{1-\eta} + \frac{1}{2}, \qquad C = \xi_x - \xi_y, \qquad D = \xi_x + \xi_y. \tag{31}$$

In reference [1], a numerical method is introduced in detail that helps to find the solution of this system. Using a modified version of Eq. (22) (we sum up the squares of absolute values of four components instead of two components), we calculate LDOS from this solution. For different numbers of the defects in the conical tip, we see the resulting LDOS in **Figure 11**. It involves the modes $j = -1, 0, 1, 2, 3$ with the same weight. While for the case of one and two defects in the tip, arbitrary energy and $r = 0$, LDOS grows to infinity, in the case of three defects in the tip, this effect appears close to zero energy only. Using a more thorough analysis, one

could find out that the peak for the case of three defects corresponds to the case of the mode *j* = −1 and for other modes and the same number of defects, the behavior is the same as in the case of one and two defects.

From these results follows that there could be a strong localization of the electrons in the tip, especially near zero energy in the case of three defects. Now, we will be interested, if this behavior remains the same after the inclusion of some boundary effects that should simulate the real geometry of the nanostructure. Furthermore, we would like to ensure in this way the quadratical integrability of the solution.
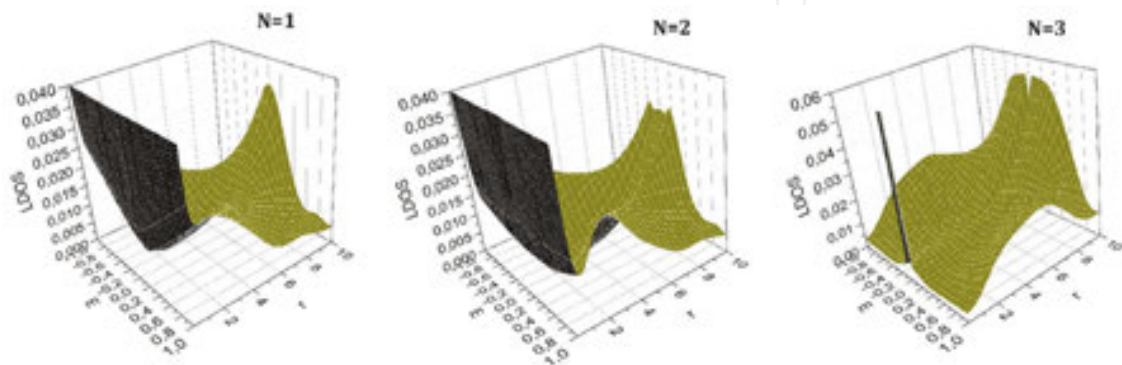
Figure 11. Three-dimensional graphs of LDOS of the graphitic nanocone influenced by SOC. Here, LDOS corresponds to the sum of the solutions corresponding to *j* = 1,0,1,2,3. The number of the defects in the tip in the particular cases: *N* = 1 (left), *N* = 2 (middle) and *N* = 3 (right).

3.2. Incorporation of the boundary effects by a charge simulation

The influence of the charge considered in the conical tip is expressed in the Hamiltonian by the presence of the diagonal term $-\frac{\kappa}{r}$, where $\kappa = 1/137$ is the fine structure constant. This term substitutes the diagonal zeros in Eq. (30):

$$\begin{pmatrix} -\dfrac{\kappa}{r} & 0 & \partial_r + \dfrac{F}{r} & -\dfrac{i}{r}C \\[2mm] 0 & -\dfrac{\kappa}{r} & -\dfrac{i}{r}D & \partial_r + \dfrac{F}{r} \\[2mm] -\partial_r + \dfrac{F-1}{r} & \dfrac{i}{r}D & -\dfrac{\kappa}{r} & 0 \\[2mm] \dfrac{i}{r}C & -\partial_r + \dfrac{F-1}{r} & 0 & -\dfrac{\kappa}{r} \end{pmatrix} \begin{pmatrix} f_{j\uparrow,c}(r) \\[1mm] f_{j\downarrow,c}(r) \\[1mm] g_{j\uparrow,c}(r) \\[1mm] g_{j\downarrow,c}(r) \end{pmatrix} = E \begin{pmatrix} f_{j\uparrow,c}(r) \\[1mm] f_{j\downarrow,c}(r) \\[1mm] g_{j\uparrow,c}(r) \\[1mm] g_{j\downarrow,c}(r) \end{pmatrix}. \tag{32}$$

In this way, the parallel influence of both the Coulomb interaction and SOC is considered [3]. To solve the resulting equation, we use the analogy of the numerical method used in [1]—this analogy is presented in reference [3]. From the calculated results, LDOS is calculated using Eq. (22) again.

The graphs of LDOS based on the found solution are sketched in **Figure 12** for the same modes and numbers of the defects as in **Figure 11**, i.e., $-1 \leq j \leq 3$. In spite of our expectations, this time the behavior of the found result is the same for arbitrary number of the defects, i.e., the appearance and the uniqueness of the peak in the case of three defects are distorted.
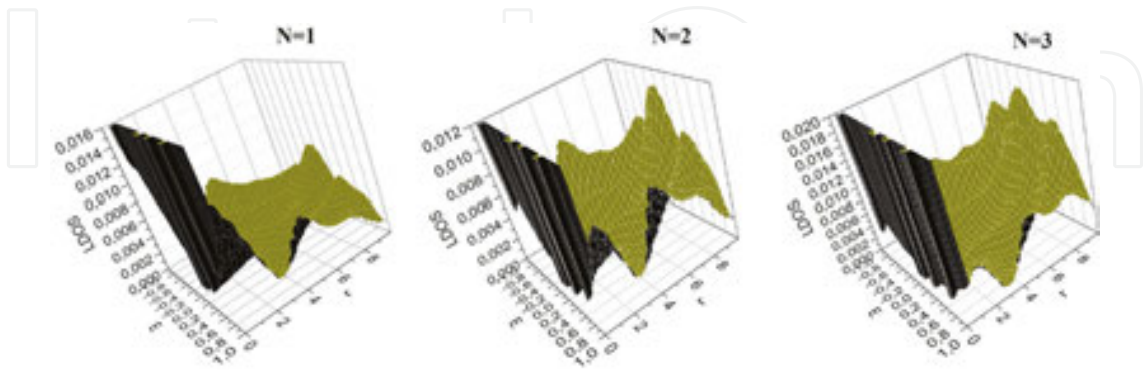
Figure 12. Graphs of LDOS of the graphitic nanocone influenced by the Coulomb interaction (including the influence of SOC) for different distances $\bar{r}$ from the tip, $-1 \leq j \leq 3$ and for different numbers of the defects.

3.3. Comparison of the results

Now, we would like to verify the possible quadratic integrability of the solution found for the case of the additional effect coming from the charge simulation. In **Figure 13**, we see the dependence of LDOS on $\bar{r}$ variable close to zero energy for the case of the influence of SOC only and of the simultaneous influence of SOC and the Coulomb interaction. We see here that in comparison with the first case, in the second case, the decrease of LDOS close to $r = 0$ is much faster and one could suppose that the quadratic integrability of the acquired solution is achieved here. To gain confidence with our conclusion, we have to do the integration of LDOS in the investigated interval close to $r = 0$ in all the outlined cases. This task is still in progress.
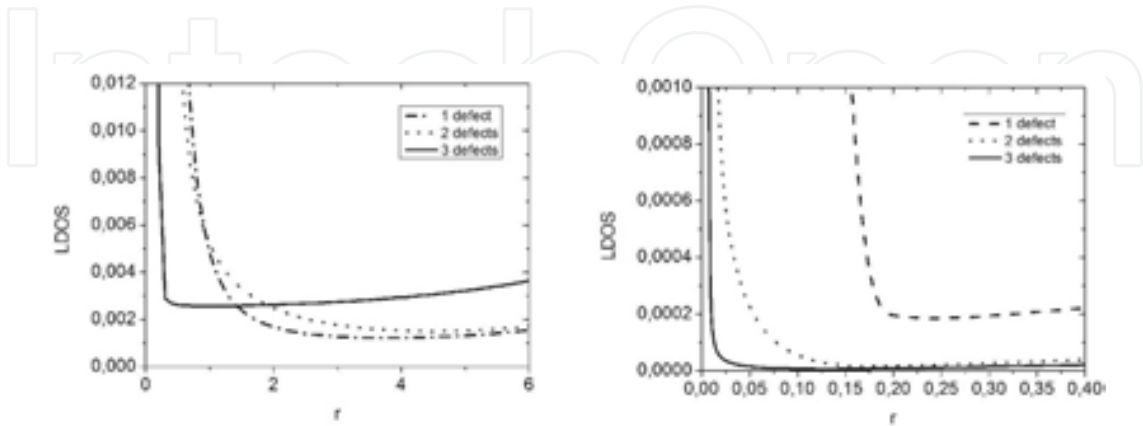
Figure 13. Behavior of LDOS for zero energy close to $r = 0$ for different numbers of defects in the conical tip: influence of SOC only (left) and the simultaneous influence of SOC and the Coulomb interaction (right).

4. Properties of the graphitic wormhole

The wormhole is understood as a form that arises when two graphene sheets are connected together with the help of the connecting nanotube. This can be achieved by the supply of the heptagonal defects on both sides of the given nanotube. The number of the defects can vary from 1 to 12. The composition of the graphitic wormhole is depicted in **Figure 14**: it consists of the connecting nanotube and two (perturbed or unperturbed) graphene sheets. The places of the connections are called the wormhole bridges. Because of the physical limitations, the radius of the nanotube must be much larger than its length (this fact is ignored in **Figure 14** for the better illustration of the composition). The limit case of 12 defects is described in references [4, 17], in the other cases, we speak about the so-called "perturbed wormhole" Here, using the formalism of the subsection II B, we derive the electronic structure for both cases, and we will find out the form of the zero modes on the wormhole bridge. Furthermore, we investigate the influence of the additional effects that could appear here due to extreme curvature in the place of the wormhole bridge—the relativistic mass acquisition of the present electrons. This effect together with the effect of SOC that appears in the carbon nanotubes [16] could lead to the appearance of the zero modes of the chiral massive electrons in the place of the wormhole bridge. This could serve as a useful instrument for the detection of the wormhole structures in the graphene bilayer during the process of the synthesis of the corresponding material.
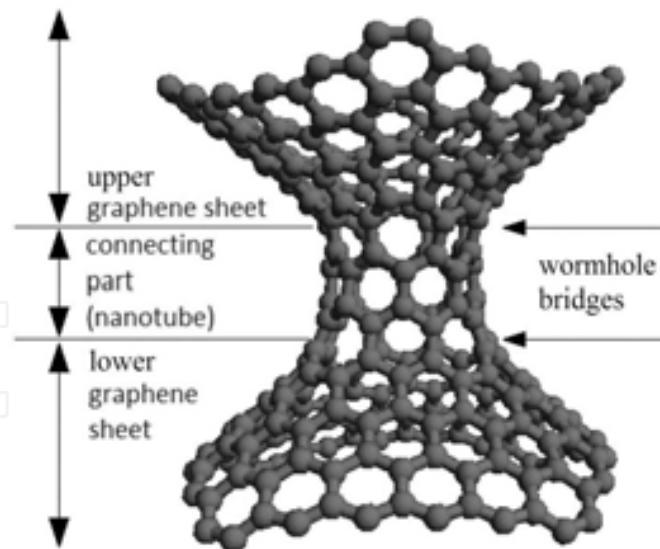
Figure 14. The composition of the graphitic wormhole.

4.1. Electronic structure

We will solve Eq. (15) in the subsection II B. In this case, the metric tensor has the form

$$g_{\mu\nu} = \Lambda^2(r_\pm)\begin{pmatrix} 1 & 0 \\ 0 & r_\pm^2 \end{pmatrix}, \qquad \Lambda(r_\pm) = \left(a/r_\pm\right)^2 \theta(a - r_\pm) + \theta(r_\pm - a). \qquad (33)$$

Here, θ is the Heaviside step function, r_-, r_+ are the polar coordinates corresponding to the lower and the upper graphene sheet, respectively and $a = \sqrt{r_- r_+}$ is the radius of the wormhole.

The values of the components of a_μ depend on the chiral vector [18] of the connecting nanotube. For our purpose, this vector is $(6n, 6n)$ and $(6n, 0)$. In most cases, a_μ has then the components

$$a_\varphi = \frac{3}{2}, \qquad a_r = 0. \qquad (34)$$

The only exception is when the chiral vector is $(6n, 0)$, where n is not divisible by 3. Then,
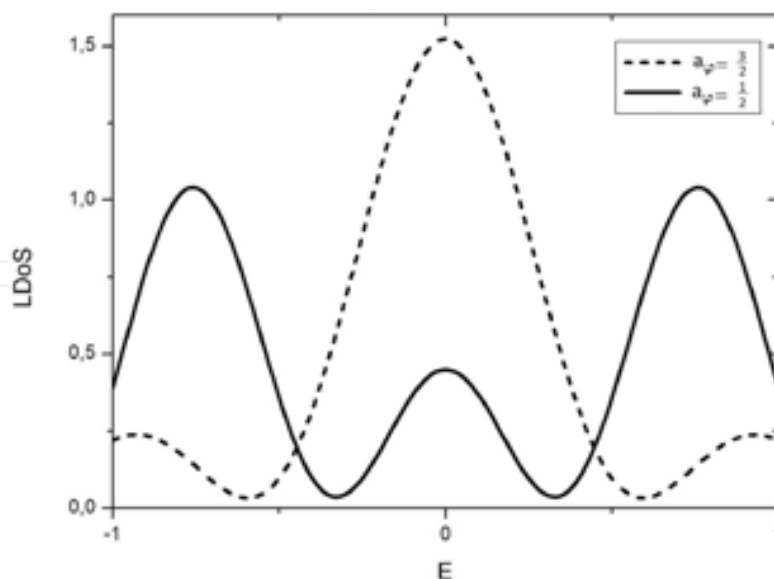
$$a_\varphi = \frac{1}{2}, \qquad a_r = 0. \qquad (35)$$

Knowledge of the spin connection is also needed—the values of the components have the form

$$\Omega_\varphi = -\frac{i}{2}\sigma_3\left(r\frac{\Lambda'(r)}{\Lambda(r)} + 1\right), \qquad \Omega_r = 0. \qquad (36)$$

All these expressions we substitute into Eq. (15). The resulting equation is

$$iv_F \sigma^\mu(\partial_\mu + \Omega_\mu \mp ia_\mu)\psi^\pm = \varepsilon\psi^\pm. \qquad (37)$$

Figure 15. Local density of states on the bridge of the graphitic wormhole for different values of a_φ.

Here, each sign $\pm$ corresponds to a different Dirac point (the corner of the reciprocal unit lattice). We get these four possibilities: for $r \geq a$,

$$-\mathrm{i}v_F\left(\partial_r + \frac{1}{r}\mathrm{i}\partial_\theta \mp \frac{a_\varphi}{r} + \frac{1}{2r}\right)\psi_B^\pm = \varepsilon\psi_A^\pm, \qquad -\mathrm{i}v_F\left(\partial_r - \frac{1}{r}\mathrm{i}\partial_\theta \pm \frac{a_\varphi}{r} + \frac{1}{2r}\right)\psi_A^\pm = \varepsilon\psi_B^\pm \qquad (38)$$

and for $0 < r \le a$,

$$\mathrm{i}v_F\left(\frac{r}{a}\right)^2\left(\partial_r - \frac{1}{r}\mathrm{i}\partial_\theta \pm \frac{a_\varphi}{r} - \frac{1}{2r}\right)\psi_B^\pm = \varepsilon\psi_A^\pm, \qquad \mathrm{i}v_F\left(\frac{r}{a}\right)^2\left(\partial_r + \frac{1}{r}\mathrm{i}\partial_\theta \mp \frac{a_\varphi}{r} - \frac{1}{2r}\right)\psi_A^\pm = \varepsilon\psi_B^\pm. \qquad (39)$$

In the first case, the solution is

$$\psi^\pm = \begin{pmatrix} \psi_A^\pm(r,\varphi) \\ \psi_B^\pm(r,\varphi) \end{pmatrix} = c_1\begin{pmatrix} J_{j\mp a_\varphi - 1/2}(kr) \\ -\mathrm{i}\,\mathrm{sgn}\varepsilon\, J_{j\mp a_\varphi + 1/2}(kr) \end{pmatrix}$$
$$+ c_2\begin{pmatrix} Y_{j\mp a_\varphi - 1/2}(kr) \\ -\mathrm{i}\,\mathrm{sgn}\varepsilon\, Y_{j\mp a_\varphi + 1/2}(kr) \end{pmatrix}. \qquad (40)$$

Here, $J_j(x)$ and $Y_j(x)$ are the Bessel functions of the integer order j and the energy $\varepsilon = \pm v_F k$. To calculate LDOS, similarly as in the previous section, Eq. (22) is used. In **Figure 15**, different behavior of LDOS, depending on the gauge field a_φ, is manifested.

4.2. Zero modes

For the presented possibilities, we investigate the zero modes—solutions of the Dirac equation for the zero energy. For this purpose, we consider zero values of the component $\psi_A^\pm$ of the solution. Then, from Eqs. (49) and (50) follows: for $r \ge a$,
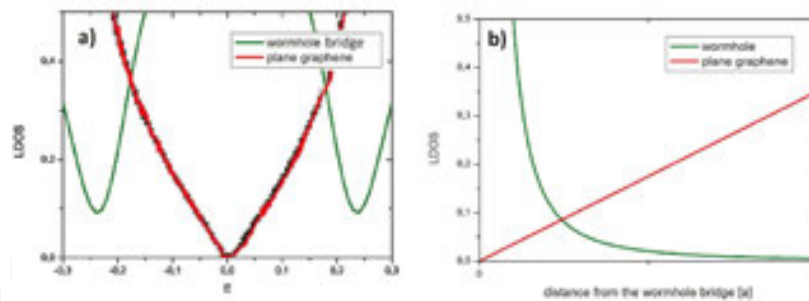
Figure 16. Comparison of the properties of the wormhole and the plain graphene: (a) local density of states, (b) zero modes.

$$\left(\partial_r - \frac{1}{r}\mathrm{i}\partial_\theta \mp \frac{a_\varphi}{r} + \frac{1}{2r}\right)\psi_B^\pm = 0 \qquad (41)$$

and for $0 < r \le a$,

$$\left(\partial_r - \frac{1}{r}\mathrm{i}\partial_\theta \pm \frac{a_\varphi}{r} - \frac{1}{2r}\right)\psi_B^\pm = 0. \qquad (42)$$

If $a_\varphi = \frac{3}{2}$ and $r \ge a$, the solution is

$$\psi_B^-(r,\varphi) \sim r^{-j-2}e^{ij\varphi}.$$

(43)

The second possibility for this value of a_φ is $0 < r \le a$, the corresponding solution is then

$$\psi_B^-(r,\varphi) \sim r^{-j+2}e^{ij\varphi}.$$

(44)

Both solutions are strictly normalizable only for $j = 0$. Analogous solution holds for ψ_B^+ and for $\psi_A^\pm$ if the components $\psi_B^\pm$ are chosen as zero.

There are no strictly normalizable solutions for the value $a_\varphi = \frac{1}{2}$. It means that in this case, the zero modes do not exist.

On the base of these results, one could expect a strong localization of LDOS near Fermi energy on the wormhole bridge. It is demonstrated in **Figure 16a**, where LDOS of the plain graphene is supplied for the comparison. It could be experimentally observed. In **Figure 16b**, we see the comparison of the zero modes of these two structures at different distances from the wormhole bridge.

4.3. Case of massive fermions

In the continuum gauge field theory, zero mass of the fermions in the Dirac equation is considered (in other words, it is very small in comparison with energy). On the other hand, the extreme curvature of the investigated structure leads to such values of the Fermi velocity that cause the appearance of the relativistic effects. The changes of the Fermi velocity due to curvature and other effects were demonstrated in references [13, 19]. As a result, the mass of the fermions becomes considerable, similarly as in the bilayer graphene [20, 21]. This effect is strengthened by the effective mass acquisition during the motion along the tube axis that happens due to the extreme size difference between the graphene sheets and the wormhole radius. This change of the space topology of graphene from 2D to 1D is similar to the string theory compactification. It means that we can image the wormhole connecting nanotube as the 1D object.

So we need to incorporate a mass term into the Dirac equation (Eq. (15)). To solve this problem, we go through the system of the corresponding equations (Eq. (20)) and transform it into the following differential equation of the second order:

$$\left(\partial_{\xi\xi} - \frac{1}{2g_{\xi\xi}}\partial_\xi g_{\xi\xi} + \frac{\tilde{j}}{2}\sqrt{\frac{g_{\xi\xi}}{g_{\varphi\varphi}^3}}\partial_\xi g_{\varphi\varphi} - \tilde{j}^2 \frac{g_{\xi\xi}}{g_{\varphi\varphi}} + E^2 g_{\xi\xi} \right)u_j = 0.$$

(45)

To simplify the calculations, the cylindrical geometry is supposed: the radius vector of the point at the surface changes as

$$\vec{R} = (R\cos\varphi, R\sin\varphi, \xi), \tag{46}$$

where R is the radius of the cylinder. In this case, Eq. (45) is considerably simplified:

$$\left(\partial_{\xi\xi} + E^2 - \frac{\tilde{j}^2}{R^2}\right)u_j = 0, \tag{47}$$

which is solved by [22]

$$u_j(\xi) = Ae^{k\xi} + Be^{-k\xi}. \tag{48}$$

Here,

$$k = \sqrt{\frac{\tilde{j}^2}{R^2} - E^2}. \tag{49}$$

In references [23, 24], in a very similar form the dispersion relation is given for the massive 1D Dirac equation:

$$k = \sqrt{M^2 - E^2}, \tag{50}$$

where M is the mass of the corresponding fermion. From reference [22], an analogy indeed follows between the 2D massless and 1D massive case. On this base, we rewrite Eq. (45) into the form

$$\left(\partial_{\xi\xi} - \frac{1}{2g_{\xi\xi}}\partial_\xi g_{\xi\xi} + \frac{\tilde{j}}{2}\sqrt{\frac{g_{\xi\xi}}{g_{\varphi\varphi}^3}}\partial_\xi g_{\varphi\varphi} - \tilde{j}^2\frac{g_{\xi\xi}}{g_{\varphi\varphi}} + (E^2 - M^2)g_{\xi\xi}\right)u_j = 0, \tag{51}$$

in this case, the mass M corresponds to the fermion in the altered conditions. Now we find the corrections of LDOS of the graphitic wormhole for different values of M. It is shown in **Figure 17**. Our prediction is that these massive particles arising in the wormhole nanotubes could create energy bulks on the wormhole bridge and in the close area that should be experimentally measured by the STM or by the Raman spectroscopy [25]. Moreover, this effect could be strengthened by the effect of SOC present in the connecting nanotube that was described in reference [16] for the nanotubes and in Section 3 for the nanocone. This effect causes next energy splitting and as the result, the aforementioned chiral massive electrons could appear.

Another possibility to identify the wormhole structure comes from the fact that the massive particles could create strain solitons and topological defects on the bridge of the bilayer graphene that should propagate throughout the graphene sheet. These are almost macroscopic effects and should be caught by the experimentalists [26].
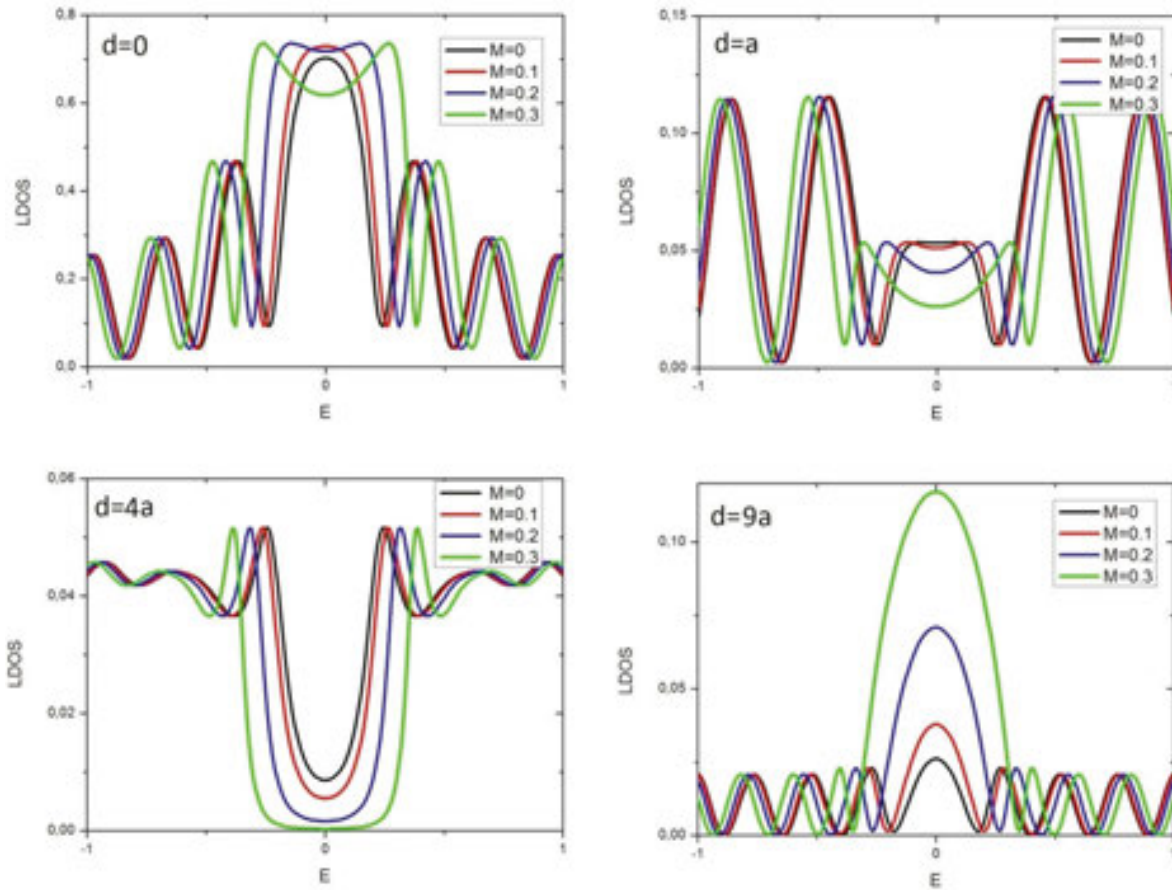
Figure 17. Comparison of LDOS for different masses of fermions at different distances from the wormhole bridge.

4.4. Case of perturbed wormhole

Now we will investigate how the electronic structure changes if the number of the heptagonal defects on the wormhole bridge is lowered—in this way, the perturbed wormhole is created.

In **Figure 18**, the possible forms of this structure are depicted. Due to symmetry preservation, only the even numbers of the defects, i.e., 2, 4, 6, 8, or 10, are considered.

The metric of the sheets can be draught by the radius vector

$$\vec{R}(z,\varphi) = \left(a\sqrt{1 + {}_{\Delta}z^2}\cos\varphi, a\sqrt{1 + {}_{\Delta}z^2}\sin\varphi, z \right), \tag{52}$$

where $\triangle$ is a positive real parameter; its value is derived from the number of the defects of the wormhole. In the case of $N = 2$ defects, we can say that the value of this parameter is negligible, so $\triangle \ll 1$. Then, the nonzero components of the metric are

$$g_{zz} = 1 + \frac{a^2 \triangle^2 z^2}{1 + \triangle z^2} \sim 1 + a^2 \triangle^2 z^2, \qquad g_{\varphi\varphi} = a^2 (1 + \triangle z^2). \qquad (53)$$

The nonzero components of the gauge fields are

$$a_\varphi = N / 4, \qquad a_\varphi^W = -(2m + n) / 3, \qquad (54)$$

(a)   (b)   (c)   (d)   (e)
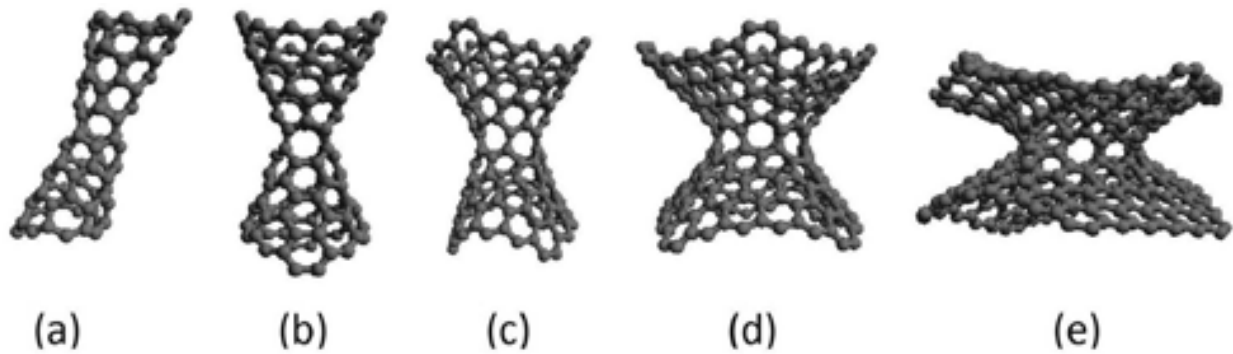
Figure 18. Different forms of the perturbed wormhole: (a) Two defects, (b) Four defects, (c) Six defects, (d) Eight defects, (e) Ten defects.

where (n, m) is the chiral vector of the connecting nanostructure. Then, regarding the form of the spin connection and by the substitution into Eq. (15), we get the solution

$$\psi_A(z) = C_{\triangle 1} D_{v_1}(\xi(z)) e^{ij\varphi} + C_{\triangle 2} D_{v_2}(i\xi(z)) e^{ij\varphi}, \qquad (55)$$

$$\psi_B(z) = \frac{C_{\triangle 1}}{E} \left(\partial_z D_{v_1}(\xi(z)) - \frac{\tilde{j} D_{v_1}(\xi(z))}{a} (1 - \frac{1}{2} \triangle^2 z^2) \right) e^{-ij\varphi}$$

$$+ \frac{C_{\triangle 2}}{E} \left(\partial_z D_{v_2}(i\xi(z)) - \frac{\tilde{j} D_{v_2}(i\xi(z))}{a} (1 - \frac{1}{2} \triangle^2 z^2) \right) e^{-ij\varphi}, \qquad (56)$$

where

$$v_1 = i\frac{a^2{}_\Delta - 4a^2 E^2 + 4ia\sqrt{_\Delta}\tilde{j} + 4\tilde{j}^2}{8a\sqrt{_\Delta}\tilde{j}}, \qquad v_2 = -i\frac{a^2{}_\Delta - 4a^2 E^2 - 4ia\sqrt{_\Delta}\tilde{j} + 4\tilde{j}^2}{8a\sqrt{_\Delta}\tilde{j}},$$ (57)

$$\xi(z) = (-_\Delta)^{1/4}\left(\sqrt{\frac{a}{2\tilde{j}}} + \sqrt{\frac{2\tilde{j}}{a}}z\right),$$ (58)

$D_v(\xi)$ being the parabolic cylinder function. The functions $C_{\Delta 1} = C_{\Delta 1}(E)$, $C_{\Delta 2} = C_{\Delta 2}(E)$ serve as the normalization constants. We see the graph of the local density of states in **Figure 19** (left part).

In the case of more than two defects, the value of Δ is not negligible, and we can get only the numerical approximation of LDOS. The derivation of the value of the parameter Δ follows from **Figure 19** (right part). From this figure it follows that in the middle part, the upper branch of the graphene sheet converges to the line $z = x \cdot \tan\alpha$, where we can suppose that the angle α depends on the number of the defects N linearly, i.e., $\alpha = \frac{\pi}{2} - N \cdot \frac{\pi}{24}$. (In this case, $\alpha = \frac{\pi}{2}$ corresponds to 0 defects and $\alpha = 0$ corresponds to 12 defects.) Simultaneously, from Eq. (52) follows that asymptotically we have

$$\vec{R}(z \to \infty, \varphi) \to \left(a\sqrt{_\Delta}z\cos\varphi, a\sqrt{_\Delta}z\sin\varphi, z\right),$$ (59)
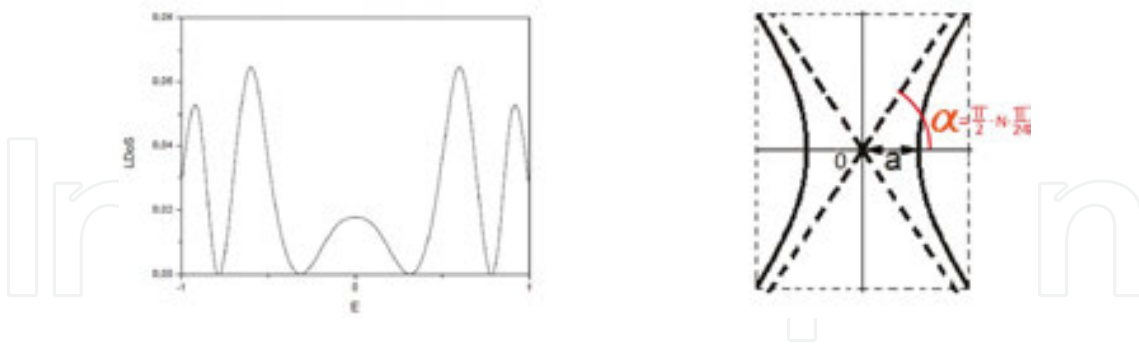
Figure 19. Left: LDOS on the bridge of the graphitic perturbed wormhole. Right: Derivation of the Δ parameter.
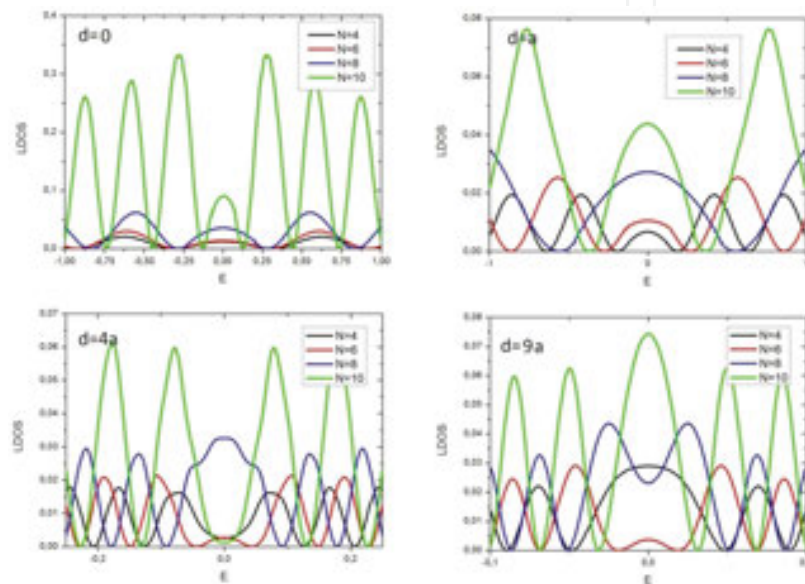
from which follows

$$z = x \cdot \tan\alpha = \left(a\sqrt{_\Delta}\right)^{-1}x,$$ (60)

so

$$\Delta = \frac{1}{a^2 \tan^2 \alpha} = \frac{1}{a^2 \tan^2 \left(\dfrac{\pi}{2} - N \cdot \dfrac{\pi}{24} \right)}. \tag{61}$$

In **Figure 20**, we see the comparison of LDOS for different kinds of the perturbed wormhole. From the plots it follows that the intensity is rising with the increasing number of the defects, and it is closer and closer approaching the results in **Figure 15**, where the case of 12 defects is shown.

Figure 20. Comparison of LDOS for different numbers of the defects in the perturbed wormhole at different distances d from the wormhole bridge.
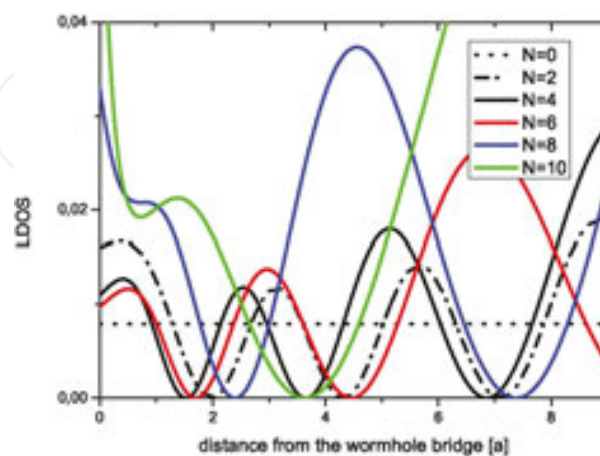
Figure 21. Zero modes of the perturbed wormhole for different numbers of the defects.

In **Figure 21**, LDOS of zero modes is shown for a varying distance from the wormhole bridge in the units of the radius a of the wormhole center. It was also acquired in the numerical way. For the unperturbed case (0 defects), the resulting plot resembles a line. In reference [27], the exponential solution is found for this case but with a very slow increase, so this could be that case. It is also seen from the plot that for the increasing number of the defects, the solution is approaching expressions in Eqs. (54) and (55) for the zero modes of the unperturbed wormhole.

Of course, the massive fermions could also appear in the case of the perturbed wormhole. We will not perform a detailed derivation of the electronic structure for the case of this eventuality, and we only note that the corrections to LDOS would be an analogy of the corrections shown in **Figure 17**.

5. Conclusion

We performed the calculations of the electronic structure for the graphitic nanocone and the graphene wormhole. In the first case, our aim was to find the quadratically integrable solution that includes the boundary effects and considers the real geometry. This goal was partially achieved, but we need to verify the properties of the found solution close to the tip. The precision of the calculations could be improved by the better choice of the corresponding geometry, by the consideration of the discretion of the energetic spectrum coming from the finite size of the nanostructure, and by the inclusion of next effects coming from the overlap of the neighboring atomic orbitals close to the tip [2]. The localization of the electrons shown in **Figures 11** and **12**, especially in the case of three defects, makes the graphitic nanocone a possible candidate for the construction of the scanning probe in atomic force microscopy.

In the second case of the graphene wormhole, we presented the mathematical motivation for our prediction of the effects that should appear close to the wormhole bridge. Our predictions will be verified with the help of the geometric optimizations and ab initio calculations. On this base, the most suitable candidates for the experiments will be chosen.

Author details

Jan Smotlacha[1,2*] and Richard Pincak[3,1]

*Address all correspondence to: smota@centrum.cz

1 Bogoliubov Laboratory of Theoretical Physics, Joint Institute for Nuclear Research, Dubna, Moscow region, Russia

2 Faculty of Nuclear Sciences and Physical Engineering, Czech Technical University, Brehova, Prague, Czech Republic

3 Institute of Experimental Physics, Slovak Academy of Sciences, Kosice, Slovak Republic

References

[1] Pincak R, Smotlacha J, Pudlak M. Spin-orbit interaction in the graphitic nanocone. Eur. Phys. J. B. 2015;88:17–22. DOI: 10.1140/epjb/e2014-50413-9

[2] Pincak R, Smotlacha J, Pudlak M. Calculation of the electronic structure near the tip of a graphitic nanocone. Physica B. 2014;441:58–61. DOI: 10.1016/j.physb.2014.02.012

[3] Smotlacha J, Pincak R. Boundary conditions and Green function approach of the spin-orbit interaction in the graphitic nanocone [Internet]. 2015. Available from: http://arxiv.org/abs/1511.03004. [Accessed: 2015-11-10]

[4] Gonzalez J, Guinea F, Herrero J. Propagating, evanescent, and localized states in carbon nanotube-graphene junctions. Phys. Rev. B. 2009; 79:165434. DOI: 10.1103/PhysRevB.79.165434

[5] Pincak R, Smotlacha J. Analogies in electronic properties of graphene wormhole and perturbed nanocylinder. Eur. Phys. J. B. 2013;86:480–486. DOI: 10.1140/epjb/e2013-40594-0

[6] Pincak R, Smotlacha J. The chiral massive fermions in the graphitic wormhole. Quantum Matter. 2016; 5:114–124. DOI: 10.1166/qm.2016.1262

[7] Wallace PR. The band theory of graphite. Phys. Rev. 1947;71:622–634. DOI: 10.1103/PhysRev.71.622

[8] Slonczewski JC, Weiss PR. Band structure of graphite. Phys. Rev. 1958;109:272–279. DOI: 10.1103/PhysRev.109.272

[9] Pincak R, Smotlacha J, Osipov VA. Electronic states of zigzag graphene nanoribbons with edges. Physica B. 2015;475:61–65. DOI: 10.1016/j.physb.2015.06.025

[10] Wakabayashi K, Sasaki K, Nakanishi T, Enoki T. Electronic states of graphene nanoribbons and analytical solutions. Sci. Technol. 2010;11:054504 DOI: 10.1088/1468-6996/11/5/054504

[11] DiVincenzo DP, Mele EJ. Self-consistent effective-mass theory for intralayer screening in graphite intercalation compounds. Phys. Rev B. 1984;29:1685–1694 DOI: 10.1103/PhysRevB.29.1685

[12] Callaway J. Quantum Theory of the Solid State. New York: Academic Press;1974. 824 p. DOI: 10.1107/S0567739478000662

[13] Kochetov EA, Osipov VA, Pincak R. Electronic properties of disclinated flexible membrane beyond the inextensional limit: application to graphene. J. Phys. Condens. Matter. 2010;22:395502. DOI: 10.1088/0953-8984/22/39/395502

[14] Smotlacha J, Pincak R, Pudlak M. Electronic structure of disclinated graphene in an uniform magnetic field. Eur. Phys. J. B. 2011;84:255–264. DOI: 10.1140/epjb/e2011-20384-6

[15] Sitenko YA, Vlasii ND. Electronic properties of graphene with a topological defect. Nucl. Phys. B. 2007;787:241–259. DOI: 10.1016/j.nuclphysb.2007.06.001

[16] Ando T. Spin-orbit interaction in carbon nanotubes. J. Phys. Soc. Jpn. 2000;69:1757–1763. DOI: 10.1143/JPSJ.69.1757

[17] Gonzalez J, Herrero J. Graphene wormholes: a condensed matter illustration of Dirac fermions in curved space. Nucl. Phys. B. 2010;825:426–443. DOI: 10.1016/j.nuclphysb.2009.09.028

[18] Saito R, Dresselhaus G, Dresselhaus MS. Tunneling conductance of connected carbon nanotubes. Phys. Rev. B. 1996;53:2044–2050. DOI: 10.1103/PhysRevB.53.2044

[19] Rostami H, Asgari R. Electronic ground-state properties of strained graphene. Phys. Rev. B. 2012;86:155435. DOI: 10.1103/PhysRevB.86.155435

[20] Borghi G, Polini M, Asgari R, MacDonald AH. Fermi velocity enhancement in monolayer and bilayer graphene. Solid State Commun. 2009;149:1117–1122. DOI: 10.1016/j.ssc.2009.02.053

[21] Katsnelson MI, Novoselov KS, Geim AK. Chiral tunnelling and the Klein paradox in graphene. Nature Phys. 2006;2:620–625. DOI: 10.1038/nphys384

[22] Alhaidari AD, Jellal A, Choubabi EB, Bahlouli H. Dynamical mass generation via space compactification in graphene. Quantum Matter. 2013;2:140–143. DOI: 10.1166/qm.2013.1039

[23] Greiner W. Relativistic Quantum Mechanics: Wave Equations. 3rd ed. Berlin: Springer; 1994. 424 p. DOI: 10.1007/978-3-662-04275-5

[24] Thaller B. The Dirac Equation. 1st ed. Springer, Berlin: Springer;1992. 357 p. DOI: 10.1007/978-3-662-02753-0

[25] Tan PH et al. The shear mode of multilayer graphene. Nature Mater. 2012;11:294–300. DOI: 10.1038/nmat3245

[26] Alden JS, Tsen AW, Huang PY, Hovden R, Brown L, Park J, Muller DA, McEuen PL. Strain solitons and topological defects in bilayer graphene [Internet]. 2013. Available from: http://arxiv.org/abs/1304.7549. [Accessed: 2013-04-29]

[27] Pincak R, Smotlacha J, Pudlak M. Electronic properties of disclinated nanostructured cylinders. NanoMMTA. 2013; 2:81–95. DOI: 10.2478/nsmmt-2013-0005